Nanoscale

PAPER

View Article Online
View Journal | View Issue

Cite this: *Nanoscale*, 2018, **10**, 6602

Upconversion thermometry: a new tool to measure the thermal resistance of nanoparticles†

O. A. Savchuk,[a] J. J. Carvajal,[a]* C. D. S. Brites,[b] L. D. Carlos,[b]* M. Aguilo[a] and F. Diaz[a]

Received 23rd November 2017,
Accepted 3rd March 2018

DOI: 10.1039/c7nr08758f

rsc.li/nanoscale

The rapid evolution in luminescence thermometry in the last few years gradually shifted the research from the fabrication of more sensitive nanoarchitectures towards the use of the technique as a tool for thermal bioimaging and for the unveiling of properties of the thermometers themselves and of their local surroundings, for example to evaluate heat transport at unprecedented small scales. In this work, we demonstrated that $KLu(WO_4)_2$:Ho^{3+},Tm^{3+} nanoparticles are able to combine controllable heat release and upconversion thermometry permitting to estimate its thermal resistance (in air), a key parameter to model the heat transfer at the nanoscale.

Introduction

The emergence of luminescence nanothermometry during the last decade opened up the possibility of measuring thermal flows at spatial scales below 10 μm, unreachable by conventional electrical methods.[1] In fact, diverse phosphors capable of providing a contactless thermal reading through their light emission properties have been examined, *e.g.*, polymers,[2] DNA or protein conjugated systems,[3] organic dyes,[4] quantum dots,[5] Cr^{3+}-based materials,[6] and trivalent lanthanide (Ln^{3+}) ions incorporated into organic–inorganic hybrids,[7] multifunctional heater-thermometer nanoplatforms,[8–10] and upconverting,[11–13] downconverting[14] and downshifting[15,16] nanoparticles. The implementation of these Ln^{3+}-based phosphors as ratiometric thermometers was extensively reviewed in the past five years for diverse applications.[17–24]

In the last couple of years, the focus of luminescence thermometry has gradually shifted from the fabrication of more sensitive nanoarchitectures towards the use of the technique as a tool for thermal bioimaging (acquisition of *in vivo* thermal images[25,26] and subcutaneous thermal videos[27] and *in vivo* ischemia detection in small animals[28]) and for the unveiling of properties of the thermometers themselves and of their local surroundings, as, for instance, the heat transfer in heater-thermometer nanoplatforms,[29] the absorption coefficient and thermal diffusivity of tissues,[30] the instantaneous ballistic velocity of Brownian nanocrystals suspended in both aqueous and organic solvents,[31] and the thermal conductivity of porous silica and titania nanostructures.[32] Thermal heating of nanoparticles (nanoheaters), induced either by the application of an alternating magnetic field or by irradiation with a near infrared (NIR) laser, has found significant applications in nanomedicine, as, for instance, magnetic hyperthermia (or magnetothermal therapy)[33,34] and photothermal therapy.[35–37] Concerning the last two examples, in which malignant cells are destroyed by intracellular thermal ablation and the tumour microenvironment is thermally-modulated to have synergic effects with standard cancer treatments, the accurate measurement of the surface-temperature of nanoheaters by using a nanothermometer is crucial for regulating the heat released to the surroundings, allowing the adjustment of the irradiation parameters, thus assisting the therapy. Although distinct nanomaterials have been designed and fabricated as nanoheaters for magnetothermal and photothermal therapies,[33,34,36,38] single heater-thermometer nanoplatforms operating in the biological spectral windows of the tissues where the absorption of water and biological specimens is minimal, and combining (i) efficient light-to-heat or magnetic field-to-heat energy conversion (>50%), (ii) high relative thermal sensitivity (>1% K^{-1}), and (iii) low temperature uncertainty (<0.1 K) have not yet been realized, despite the numerous attempts reported in the last five years.[8,29,39–42]

Wawrzynczyk *et al.*,[39] Debasu *et al.*[40] and Piñol *et al.*[29] were pioneers in combining heat generation and noncontact optical temperature sensing in single nanoplatforms using,

[a]*Universitat Rovira i Virgili, Departament Quimica Fisica i Inorganica, Fisica i Cristal·lografia de Materials i Nanomaterials (FiCMA-FiCNA)-EMaS, Campus Sescelades, E-43007, Tarragona, Spain. E-mail: joanjosep.carvajal@urv.cat*
[b]*Department of Physics, CICECO – Aveiro Institute of Materials, University of Aveiro, Campus Universitário de Santiago, 3810-193 Aveiro, Portugal. E-mail: lcarlos@ua.pt*

†Electronic supplementary information (ESI) available: XRD, TEM, elemental analysis, upconversion, thermometric characterization, photothermal heating efficiency, and temperature-time dependence for the irradiated particles. See DOI: 10.1039/c7nr08758f

Table 1 Comparison of illustrative Ln^{3+}-doped systems used in luminescence nanothermometry operating in the I-BW. The temperature range (ΔT), the excitation wavelength (λ_{exc}), the emission wavelengths used to define Δ, and the reported S_m and δT_{min} values are presented for comparison

Material	ΔT (K)	λ_{exc} (nm)	Δ	S_m (% K^{-1})	δT_{min} (K)	Ref.
Upconversion						
$KLu_{0.94}Ho_{0.01}Tm_{0.05}(WO_4)_2$ [a]	300–333	808	I_{696}/I_{755}	1.86	0.3	This work
$KLu_{0.84}Ho_{0.01}Tm_{0.15}(WO_4)_2$ [a]	300–333	808	I_{696}/I_{755}	2.84	0.2	This work
$GdVO_4@SiO_2$:Tm^{3+},Yb^{3+}	298–333	980	I_{700}/I_{800}	0.94	0.4	43
$LiNbO_3$:Tm^{3+},Yb^{3+}	323–723	980	I_{700}/I_{800}	3.00	—	44
Downshifting						
$LiLaP_4O_{12}$:Cr^{3+},Nd^{3+} [b]	123–473	665	$I_{820-840}/I_{1048}$	4.89	—	45
Gd_2O_3:Nd^{3+} [b]	288–323	580	I_{824}/I_{892}	1.75	0.1	15
LaF_3:Nd^{3+}	283–333	808	I_{865}/I_{885}	0.26	—	42
$LiLaP_4O_{12}$:Nd^{3+}	80–600	808	I_{866}/I_{870}	0.22	1.1	46
YAG:Nd^{3+}	283–343	808	I_{938}/I_{945}	0.15	—	47
$NaYF_4$:Nd^{3+}	273–423	830	I_{863}/I_{870}	0.12	—	39
SrF_2:Gd^{3+},Nd^{3+} [b]	293–338	573	I_{859}/I_{867}	0.61	2.0	48
CaF_2:Gd^{3+},Nd^{3+} [b]	293–338	573	I_{1058}/I_{867}	0.12	1.8	49
$NaNdF_4@NaYF_4@NaYF_4$:Nd^{3+}	77–550	808	I_{857}/I_{863}	0.11	—	50

[a] Emission wavelength out of the I-BW. [b] Excitation wavelength out of the I-BW.

respectively, heavily Nd^{3+}-doped $NaYF_4$ heater/thermometer nanoparticles metallic heaters combined with Yb^{3+}/Er^{3+} luminescent thermometers and magnetic heaters combined with Eu^{3+}/Tb^{3+} luminescent thermometers. The latter two examples operate using the visible emission lines of the Er^{3+} and Eu^{3+}/Tb^{3+} ions, respectively, thus, out of the first biological window (I-BW, 700–980 nm (ref. 36)). In contrast, Nd^{3+}-based nanostructures can simultaneously generate heating through photothermal conversion and temperature reading using intra-$4f^3$ emissions with energies within the first, second and third biological spectral windows.[35,39,51] However, the relative thermal sensitivity of the Nd^{3+}-based nanostructures is generally one order of magnitude lower than the typical values reported for Yb^{3+}/Er^{3+} and Eu^{3+}/Tb^{3+} luminescent thermometers (Table 1 and ref. 20 and 51). Moreover, temperature uncertainties and photothermal conversion values were scarcely evaluated.[50,52]

Here, we report the synthesis and thermal characterization of Ho^{3+}, Tm^{3+} co-doped $KLu(WO_4)_2$ nanoparticles as new multifunctional heater-thermometer nanoplatforms operating in the I-BW with an unprecedented performance: relative thermal sensitivity of 2.8% K^{-1}, temperature uncertainty of 0.2 K (both at 300 K) and photothermal efficiency of 34 ± 2% (integrating sphere method[53]) or 41 ± 3% (thermal relaxation method[54]). Moreover, as an added benefit, we demonstrate how upconversion thermometry can be used to calculate the thermal resistance of the nanoparticles in air through a full non-contact heating and temperature reading. The value obtained, 9.84×10^7 K W^{-1}, is similar to those reported for Si nanorods and Si-based heterostructured nanowires using conventional techniques. The thermal resistance of a nanostructured material is a key parameter to understand thermal transport in a large variety of technologies, such as, micro- and nanoelectronic devices, thin-film thermoelectrics, and nanoparticle-based thermal interface materials.[55]

Experimental details

Photoluminescence

The emission spectra were acquired using an integrating sphere (Labsphere, 4P-GPS-020-SL), exciting with 0.100 W using a 200×10^{-6} m core diameter fiber-coupled laser diode (Apollo Instruments, F25-808-2) emitting at 808 nm. The laser was collimated to a spot diameter of 3.0×10^{-3} m on the sample. The emission was collected using an optical spectrum analyzer (OSA, Yokogawa, AQ6373). All the samples were measured after being compacted in the bottom of a borosilicate flat bottom vial.

For the temperature-dependent experiments, the samples were in contact with a heating stage (Linkam, THMS 600) equipped with a boron disk (to obtain an improved temperature distribution). The nanoparticles were excited by the fiber-coupled diode laser with the beam focused on the sample using a 40× microscope objective (0.6 numerical aperture, spot size of $\sim 20 \times 10^{-6}$ m). The emission was collected using the same objective and the optical spectrum analyzer, after eliminating the scattered excitation radiation by using a 800 nm shortpass dichroic filter (Edmund Optics).

Time-dependent photoluminescence experiments were implemented using a portable spectrometer (MAYA 2000Pro, Ocean Optics). The spectrometer is controlled by a homebuilt MatLab© interface to record the real-time dependence of the emission spectra and the 696 and 755 nm intensities, with a time step of 0.250 s. The laser power is 1.0 W and the spot size is 20×10^{-6} m, corresponding to a power density of 318×10^6 W m^{-2}.

Transmission electron microscopy

Transmission electron microscopy (TEM) was performed in a JEOL JEM-1011 microscope placing a drop of the nanopowders, previously mixed in ethanol (Merck, pro analysis 99.8%),

on a copper grid covered by a holey carbon film (HD200 Copper Formvar/carbon).

Photothermal conversion efficiency

The photothermal conversion efficiency (η), *e.g.*, the portion of light absorbed by the nanoparticles that is transformed into heat, has been determined by two different methods: (i) the thermal relaxation method,[54] and (ii) the integrating sphere method.[53] In the first method, 0.3×10^{-3} L of an aqueous suspension of nanoparticles (1 g L^{-1}) were introduced in a glass cuvette (101-QS, Hellma Analytics). The suspension was irradiated with a Lumics fiber-coupled diode laser (LU0808 M250) emitting at 808 nm with an excitation power of 0.200 W. The laser beam was focused on the cuvette with a collimating lens, allowing a beam diameter of 5×10^{-3} m on the sample (corresponding to a power density of 10.2×10^{3} W m^{-2}). The temperature of the sample was recorded until the steady-state temperature was reached by means of a digital multimeter connected to a small Pt-100 thermo-resistor located inside the cuvette. When using the integrating method sphere, the cuvette containing the same suspension of nanoparticles was placed inside the integrating sphere, perpendicularly to the collimated 808 nm laser beam (again with a laser power density of 10.2×10^{3} W m^{-2}). A baffle was introduced inside the integrating sphere, between the sample and the detector, to prevent the direct reflections from the sample to the detector. The power values were measured by using a stabilized thermal power meter (S302C, Thorlabs).

Synthesis

$KLu_{1-x-y}Ho_xTm_y(WO_4)_2$ nanoparticles with molar concentrations x = 0.01, 0.03, 0.05 and y = 0.05, 0.10, 0.15 were synthesized by the modified Pechini sol–gel method,[56] following the methodology previously reported to prepare $KLu(WO_4)_2$:Yb^{3+},Ho^{3+} nanoparticles.[57] Briefly, Ho_2O_3 (99.9999%), Tm_2O_3 (99.9%) and Lu_2O_3 (99.9999%), used as starting reagents, were dissolved in hot nitric acid in stoichiometric proportions to form the nitrate precursors that were subsequently dissolved in distilled water with citric acid (CA), as the chelating agent, in a molar ratio [CA]/[metals] = 1. Ammonium tungstate $(NH_4)_2WO_4$ (99.99%) and potassium carbonate K_2CO_3 (99.99%) were added to the aqueous solution that was heated at 353 K under magnetic stirring during a day until the complete dissolution of the reagents. Then, ethylene glycol (EG), as the esterification agent, was added to the mixture in a molar ratio [EG]/[CA] = 2. The solution was heated at 373 K to evaporate water and generate the polymeric gel. The polymeric gel was then calcined at 573 K for 3 h to obtain the precursor powders that were again calcined at 1023 K for 2 h to eliminate the organic compounds and crystallize the desired nanoparticles.

Structural and morphological characterization

The crystalline structure of the nanoparticles was investigated by powder X-ray diffraction (XRD) to confirm that the experimental procedure results in the same phase already reported.[57]

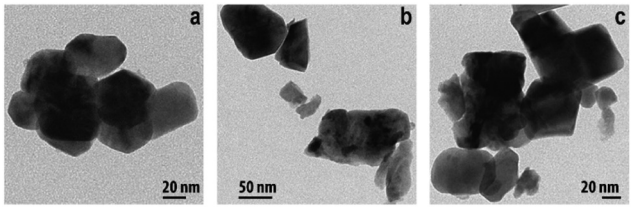

Fig. 1 TEM micrographs of $KLu_{1-x-y}Ho_xTm_y(WO_4)_2$ nanoparticles with different Ho and Tm concentrations. (a) x = 0.01 and y = 0.05, (b) x = 0.01 and y = 0.15, and (c) x = 0.05 and y = 0.05.

The XRD patterns of the $KLu_{1-x-y}Ho_xTm_y(WO_4)_2$ nanoparticles, x = 0.01, 0.03, 0.05 and y = 0.05, 0.10, 0.15, reveal that the nanoparticles crystallize in the monoclinic system with the $C2/c$ spatial group (Fig. S1 in the ESI†). The Scherrer equation was used to calculate the crystallite size. In all cases a mean size of 155 ± 10 nm was obtained indicating that, within the error of the technique, different dopant concentrations produce non-measurable changes on the crystallite size. The concentration of dopants in the nanoparticles was measured by ICP-OES (Table S1 in the ESI†). As the nominal concentration of Ho^{3+} and Tm^{3+} in the precursor powders increased, the concentration in the synthesized nanoparticles increased. Keeping the Tm^{3+} concentration constant (y = 0.05), the emission intensity is maximized for an optimal Ho^{3+} content of x = 0.03.

TEM micrographs (Fig. 1) show $KLu_{1-x-y}Ho_xTm_y(WO_4)_2$ nanoparticles with irregular shapes, typical of nanoparticles prepared using the Pechini sol–gel method,[24] with sizes around 100–150 nm, that tend to appear aggregated in small clusters. Discrete smaller particles, with sizes below 50 nm can also be seen in the images, but in a small number. No dependence of the shape or size of the nanoparticles has been observed with the concentration of doping ions used.

Results and discussion

Upconversion thermometry

The upconversion emission spectra of the $KLu_{1-x-y}Ho_xTm_y(WO_4)_2$ (x = 0.01, 0.03, 0.05 and y = 0.05, 0.10, 0.15) nanoparticles are shown in Fig. 2a and b.

The spectra consist of three separated bands located in the blue ($^1G_4 \rightarrow {}^3H_6$, Tm^{3+}), green ($^5S_2$, $^5F_4 \rightarrow {}^5I_8$, Ho^{3+}), and red ($^5F_5 \rightarrow {}^5I_8$ and $^5S_2$, $^5F_4 \rightarrow {}^5I_7$, Ho^{3+}, and $^3F_{2,3} \rightarrow {}^3H_6$, Tm^{3+}) spectral regions. The Ho^{3+} bands may be generated by Tm^{3+}-to-Ho^{3+} energy transfer processes, as previously reported.[58–60] Fig. 2c displays a simplified energy level diagram of the Ho^{3+} and Tm^{3+} ions where the represented absorption, emission and energy transfer processes are discussed in detail in the ESI.† When the molar concentration of Ho^{3+} was kept constant at x = 0.01, the intensity of all bands decreased as the concentration of Tm^{3+} increased, Fig. 2a. On the other hand, as the concentration of Ho^{3+} increased (and keeping the Tm^{3+} con-

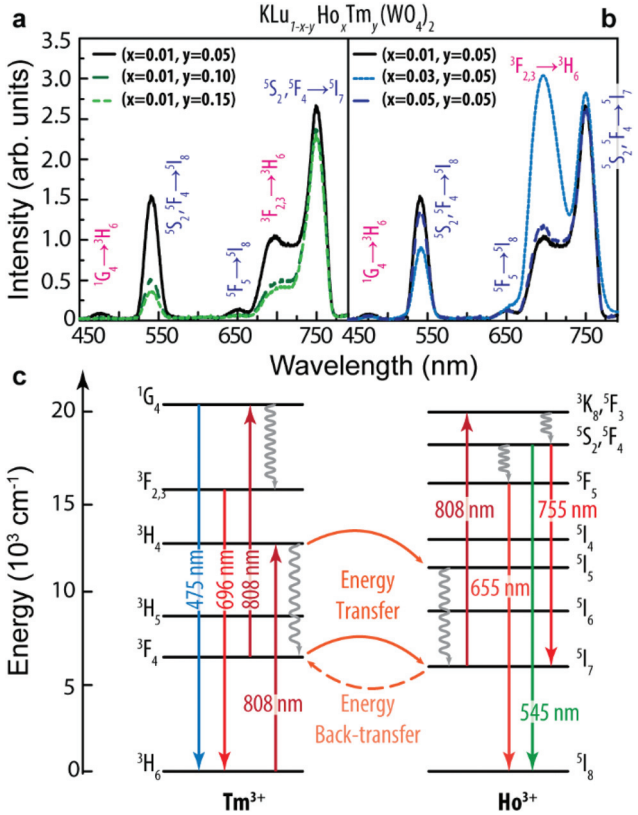

Fig. 2 Emission spectra of $KLu_{1-x-y}Ho_xTm_y(WO_4)_2$ for (a) different Tm^{3+} concentrations (keeping the Ho^{3+} concentration) and (b) different Ho^{3+} concentrations (keeping the Tm^{3+} concentration). (c) Simplified energy level diagram depicting the upconversion mechanisms for the generation of the emission spectra shown in (a). Absorption (upward arrows), radiative emission (downward arrows), non-radiative deactivations (wavy downward arrows) and energy transfer (curved arrows) processes are illustrated.

centration constant at y = 0.05), the intensity of all bands increases until x = 0.03 (Fig. 2b).

Regarding the thermometric performance of the nanoparticles, it is clear from the temperature dependent emission spectra depicted in Fig. 3a–d that the emission intensity changes significantly in the 300–330 K range and thus it can be used to measure the temperature in the I-BW. The intensity ratio (Δ) between the Tm^{3+} line centered at 696 nm (I_{696}, $^3F_{2,3} \rightarrow {}^3H_6$) and that of Ho^{3+} centered at 755 nm (I_{755}, $^5S_2$, $^5F_4 \rightarrow {}^5I_7$) was calculated in the physiological range of temperatures for all the samples (Fig. 3e). For calculation simplicity we used the intensities at 696 and 755 nm (the calculus of the integrated area of the transitions gives the same result). In the absence of a complete physical model based on the rate equations of the populations of the levels involved in the energy transfer processes depicted in Fig. 2c, the experimental points were fitted to an empirical exponential growing equation:[13,61]

$$\Delta = \Delta_0 + B\exp(\alpha T) \quad (1)$$

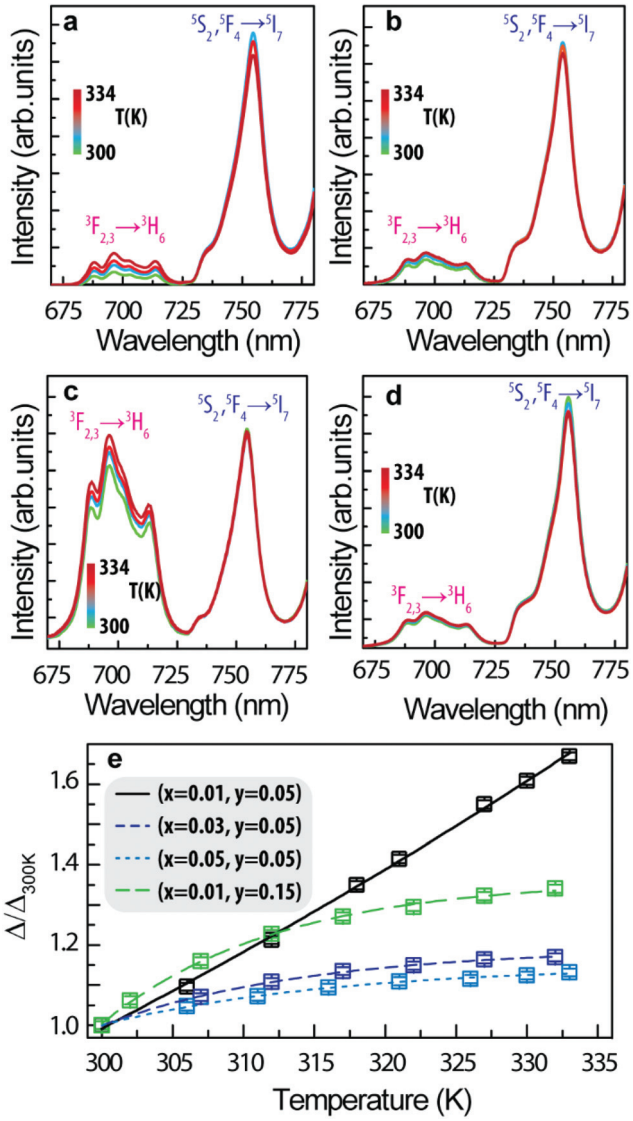

Fig. 3 Emission spectra of $KLu_{1-x-y}Ho_xTm_y(WO_4)_2$ for (a) x = 0.01 and y = 0.05, (b) x = 0.01 and y = 0.15, (c) x = 0.03 and y = 0.05, and (d) x = 0.05 and y = 0.05. (e) Intensity ratio of the emission bands located at 696 and 755 nm in the physiological range of temperatures computed from the emission spectra presented in panels a–d.

where Δ_0, B, and α are constants. We stress that the commonly used Boltzmann equation for the thermal equilibrium between two emitting states is not applicable to this intensity ratio, as it is implausible that $^3F_{2,3}$ (Tm^{3+}) and $^5S_2$,$^5F_4$ (Ho^{3+}) emitting states are in thermal equilibrium. The calibration curves are presented as lines in Fig. 3e and the corresponding fitting parameters are listed in Table S2 in the ESI.† The relative thermal sensitivity:[20]

$$S_r = \frac{1}{\Delta}\left|\frac{\partial\Delta}{\partial T}\right| = \frac{B\alpha\exp(\alpha T)}{\Delta_0 + B\exp(\alpha T)} \quad (2)$$

has been commonly used since the initial purpose by Brites *et al.*[18] in 2012 as a figure of merit to compare different

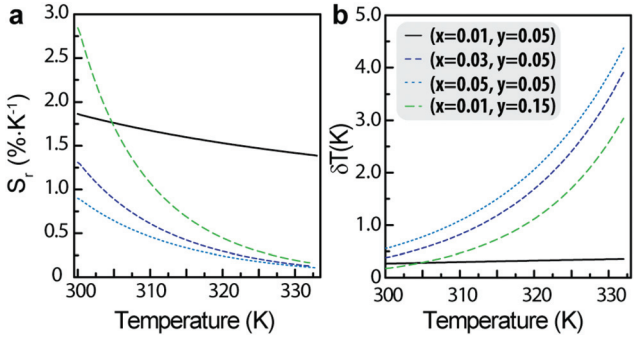

Fig. 4 (a) Relative thermal sensitivity (S_r) and (c) temperature uncertainty in the 300–330 K range of $KLu_{1-x-y}Ho_xTm_y(WO_4)_2$ nanoparticles.

thermometers, independently of their nature (Fig. 4). Table 1 compares the highest relative thermal sensitivity value (S_m) of $KLu_{0.84}Ho_{0.01}Tm_{0.15}(WO_4)_2$ and $KLu_{0.94}Ho_{0.01}Tm_{0.05}(WO_4)_2$ with those of other Ln^{3+}-doped nanoparticles with emissions in the I-BW. We selected these two samples because while the first presents the highest S_m value, the second displays an almost constant relative thermal sensitivity in all the temperature ranges studied.

Comparing with examples of Tm^{3+}, Yb^{3+} co-doped nanoparticles,[43,44] the S_m value calculated here is of the same order of magnitude. Relatively to the downshifting Nd^{3+}-doped nanoparticles,[15,39,42,46–50] however, this work presents a sensitivity value that is generally one order of magnitude larger. Not using exclusively Ln^{3+} ions, the high S_m value of the $LiLaP_4O_{12}$ nanocrystal co-doped with Cr^{3+} and Nd^{3+}, 4.89% K^{-1}, is mentioned.[45] Besides S_r, the temperature uncertainty δT is the other parameter used to characterize the nanothermometer's performance,[20] being estimated as:

$$\delta T = \frac{1}{S_r}\frac{\delta\Delta}{\Delta} = \frac{\delta\Delta}{B\exp(\alpha T)} \quad (3)$$

where $\delta\Delta/\Delta$ = 0.5% is the relative error in the determination of the thermometric parameter, a typical value of the acquisition setup used. The temperature uncertainty of the $KLu_{1-x-y}Ho_xTm_y(WO_4)_2$ nanoparticles is shown in Fig. 4b yielding a minimum temperature uncertainty value (δT_{min}) of 0.2 K, at 303 K. Table 1 compares the δT_{min} values of $KLu_{0.84}Ho_{0.01}Tm_{0.15}(WO_4)_2$ and $KLu_{0.94}Ho_{0.01}Tm_{0.05}(WO_4)_2$ with those of other Ln^{3+}-doped nanoparticles with emissions in the I-BW pointing out that our values are among the best ones reported so far.

Photothermal heating efficiency

Fig. 5 displays the temperature profile of an aqueous dispersion of $KLu_{0.84}Ho_{0.01}Tm_{0.15}(WO_4)_2$ (the sample with higher S_m value) recorded under illumination at 808 nm. In the steady-state regime (t > 600 s), we observe a maximum temperature increase (measured with the Pt-100 thermo-resistor immersed in the suspension) ($T_m - T_a$) = 8.60 ± 0.05 K (T_m and T_a are the maximum achieved temperature and the ambient temperature, respectively). As a control, the same experiment

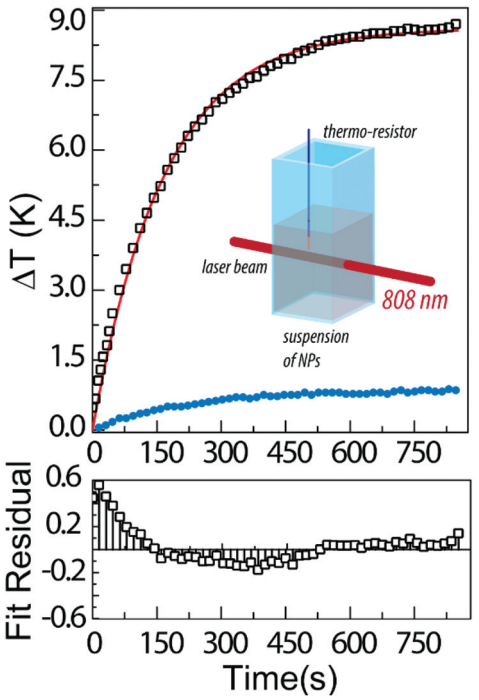

Fig. 5 Time-dependent temperature profiles of the aqueous dispersion of $KLu_{0.84}Ho_{0.01}Tm_{0.15}(WO_4)_2$ nanoparticles (squares) and of pure water (circles). The line is the fit to the experimental data using eqn (6) (r^2 > 0.994). The fit residuals are presented in the bottom graph.

was repeated for pure water, reaching a smaller maximum temperature increment (about 1.0 K, Fig. 5). This validates that the temperature increment observed in the nanoparticle's aqueous suspension is majorly due to the heat dissipation by the nanoparticles themselves (and not by the water).

The nanoparticles' photothermal conversion efficiency using the thermal relaxation method is evaluated by:[54]

$$\eta = \frac{\frac{C(T_m - T_a)}{\tau} - Q}{I(1 - 10^{-A_\lambda})} \times 100\% \quad (4)$$

where $C = \Sigma m_i c_{pi}$ is the thermal capacitance of the system (m_i and c_{pi} are, respectively, the mass and the specific heat capacity of all the i components of the system), τ is the system's thermal time constant, Q is the heat dissipated from the light absorbed by the glass cuvette and solvent, I = 0.200 W is the laser incident power, and A_λ is the absorbance of the material at λ = 808 nm. Using C = 2.936 J K^{-1}, Q = 0.08 W, A_λ = 0.959 and τ = 166.3 ± 0.7 s (from the fit shown in Fig. 5) a photothermal conversion efficiency η = 41 ± 3% is obtained (details in the ESI†).

For comparison purposes, we also determine η of the same nanoparticles as a function of the excitation power density using the integrating sphere method, a methodology described in detail elsewhere.[53] In this method η is calculated using:

$$\eta = \frac{P_b - P_s}{P_e - P_s} \times 100\% \quad (5)$$

where P_b, P_s and P_e are the power values measured for the solvent (water), sample and empty sample holder, respectively. The resulting photothermal conversion efficiency is $\eta = 34 \pm 2\%$ (mean ± std). We notice that η shows negligible dependence on the pumping power, within the range studied (Fig. S2 in the ESI†). Despite the fact that the η values obtained by the two methods are similar, that obtained with the thermal constant method is slightly higher. This is because in this method the scattered and reflected light from the sample and the walls of the cuvette in which the sample is contained is neglected, providing an overestimation of η, as pointed out before by some of us for the examples of graphene and graphene oxide flakes.[60] Although smaller than the two other values reported for Ln^{3+}-based examples, 72.1% in $NdVO_4$ NPs[52] and 72.7% in $NaNdF_4$@$NaYF_4$@1%Nd^{3+}:$NaYF_4$ multishell nanostructures,[50] the photothermal heating efficiency of our nanoparticles is higher than the values reported for metallic, Fe-based and semiconductor nanoparticles (Table 2 of ref. 34 and Table S3 in the ESI†).

Thermal resistance of the nanoparticles through upconversion thermometry

Generally, the thermal resistance of a given material (defined as the ratio between the temperature increase and the heat flowing through it) has been measured by electric means, such as the thermal bridge and thermocouples (for instance in graphene layers[62] or carbon nanotubes–Cu composites,[63] respectively) or by null-point scanning thermal microscopy (for instance in graphene disks[64]). These methods, however, overestimate the thermal resistance, since they cannot decouple the thermal resistance from the parasitic contact resistance between the nanostructures and the heat source/sink, which can typically account for 50% of the measured thermal resistance.[65] Moreover, the methods are complex, expensive and with significant limitations to be extended to other nanomaterials. Here we demonstrate that the upconversion of heater-thermometer nanoparticles can be used as a tool for the unveiling of the thermal properties of the particles themselves, in this case to determine the thermal resistance R. As an illustrative example, we use $KLu_{0.94}Ho_{0.01}Tm_{0.05}(WO_4)_2$ powder nanoparticles in contact with air. We selected this sample because their S_r and δT values are almost constant in the tested temperature interval, contrary to those of the other examples in which larger variations are observed (Fig. 4).

In a typical experiment, a laser beam is focused on the sample's surface inducing, simultaneously, upconversion emission and a temperature increment, $\Delta T(t)$, due to non-radiative deactivations. Then, the emission spectra are recorded with respect to the elapsed time being converted into temperature using eqn (1) (Fig. 6a). Fig. 6b presents the temperature increase of $KLu_{1-x-y}Ho_xTm_y(WO_4)_2$ ($x = 0.01$, $y = 0.05$ and $x = 0.01$, $y = 0.15$) induced by the irradiation with the 808 nm laser with power density values up to 400×10^6 W m^{-2}. For the same laser power density, the temperature increment is smaller for the sample with a lower Tm^{3+} concentration, suggesting a positive correlation between the heat generated

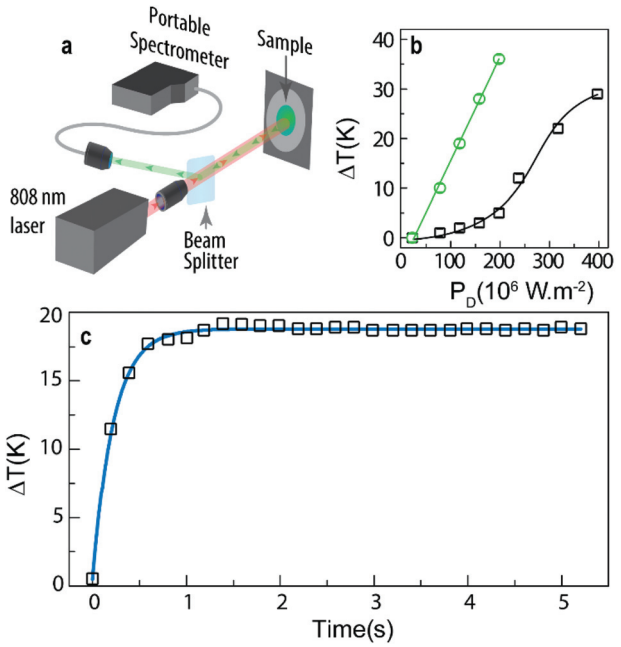

Fig. 6 (a) Scheme of the experimental setup used to measure the real-time evolution of the emission spectra upon 808 nm excitation. The laser simultaneously heats and excites the sample providing the temperature dependent upconversion emission. A beam splitter was used to redirect a part of the emitted signal to the portable spectrometer that simultaneously records the emission spectra. (b) Temperature increase induced by distinct excitation power density (P_D) for $KLu_{0.94}Ho_{0.01}Tm_{0.05}(WO_4)_2$ (black squares) and $KLu_{0.84}Ho_{0.01}Tm_{0.15}(WO_4)_2$ (green circles) powder nanoparticles in contact with air. (c) Heating curve of $KLu_{0.94}Ho_{0.01}Tm_{0.05}(WO_4)_2$ (P_D = 318 × 10^6 W m^{-2}). The solid line corresponds to the best fit to experimental data using eqn (6) (r^2 = 0.997).

due to non-radiative Tm^{3+}-to-Ho^{3+} energy transfer and Ho^{3+}-to-Tm^{3+} back transfer and the Tm^{3+} content. Moreover, the plateau discerned for high power densities (>300 × 10^6 W m^{-2}), and not observed in the P_D range studied for the sample with a higher Tm^{3+} concentration, is related to a saturation effect on the Tm^{3+} absorption at 808 nm.

The thermal gradients within the nanoparticles are negligible when compared with the temperature change in their neighborhood (Biot number lower than 0.01, details in the ESI†). Thus, the heat dissipation follows the classical Fourier law, resulting in a temperature increase given by:[66,67]

$$\Delta T(t) = \Delta T_m\left[1 - \exp\left(-\frac{hA}{mc}t\right)\right] = \Delta T_m\left[1 - \exp\left(-\frac{t}{RC}\right)\right] = \Delta T_m\left[1 - \exp\left(-\frac{t}{\tau}\right)\right] \quad (6)$$

where ΔT_m is the temperature increase in the steady-state regime (*e.g.*, in the limit $t \to \infty$) (Fig. 6c), h is the convective heat transfer coefficient, A is the thermal contact area, $R = 1/hA$ is the convective thermal resistance and $\tau = RC$. Upconversion thermometry is used to measure $\Delta T(t)$ and ΔT_m and the equivalent heating circuit is depicted in Fig. S3.†

Fitting eqn (6) to the heating curve of $KLu_{0.94}Ho_{0.01}Tm_{0.05}(WO_4)_2$ powder nanoparticles in contact with air, we obtain ΔT_m = 18.3 ± 0.2 K and τ = 0.223 ± 0.004 s (r^2 > 0.997), that corresponds to $R = (9.50 \pm 0.17) \times 10^7$ K W^{-1}, considering c = 324 J kg^{-1} K^{-1} and m estimated by multiplying the area of the excitation beam, $\pi \times 10^{-10}$ m^2, by the penetration length, 3×10^{-6} m, and the density ρ = 7686 kg m^{-3} (the c and ρ values are from the $KLu(WO_4)_2$ bulk crystal,[68,69] Table S4, ESI†).

To the best of our knowledge, this is the first report of thermal resistance values for oxide nanoparticles. Nevertheless, the calculated value is of the same order of magnitude of the measured interfacial thermal resistance across the $Si/NiSi_2$ interface in $Si_{0.7}Ge_{0.3}/NiSi_{0.7}Ge_{0.3}$ heterostructured nanowires, 6–12 × 10^7 K W^{-1},[70] and of the estimated value for interfacial thermal resistance of a 1 μm Si nanowire on an Si substrate, 0.1–10 × 10^7 K W^{-1}.[55] Interestingly, it is well known that in all applications where nanoparticles are in physical contact with a substrate, the thermal transport in these systems is expected to be dominated by the thermal resistance at the interface formed between the nanostructure and the substrate.[55]

The calculus of the τ value allows the determination of the temporal resolution of the $KLu_{0.94}Ho_{0.01}Tm_{0.05}(WO_4)_2$ thermometer (δt) which can be calculated by:[20]

$$\delta t = \frac{\delta T}{\left[\frac{\partial T}{\partial t}\right]_{max}} = \frac{\delta T}{\frac{\Delta T_m}{\tau}} \quad (7)$$

where the details of the calculus of the maximum temporal change of the temperature are shown in the ESI.† The minimum temporal resolution, δt_{min} = 0.0033 ± 0.0007 s, corresponds to the minimum temperature uncertainty (0.3 K at 300 K) and is 2–4 orders of magnitude better than those of the thermometers based on scanning thermal microscopy (0.1 s, Saïdi *et al.*,[71] and 1.5 s, Tetienne *et al.*[72] and Sedmak *et al.*[73]) and Raman spectroscopy[20] (90 s, Deshpande *et al.*[74]), being comparable to that of Eu^{3+}/Tb^{3+} luminescent molecular thermometers reported by some of us as ~0.001 s.[75,76]

Conclusions

We demonstrated that $KLu_{1-x-y}Ho_xTm_y(WO_4)_2$ (x = 0.01–0.05 and y = 0.05–0.15) nanoparticles are tunable multifunctional heater-thermometer nanoplatforms under 808 nm excitation. Additionally, the upconversion emission lines at 696 and 755 nm (in the I-BW) can be used for luminescence thermometry, with a relative maximum thermal sensitivity of 2.8% K^{-1} and a minimum temperature uncertainty of 0.2 K at 300 K. The photothermal conversion efficiency was determined by both the thermal relaxation and the integrating sphere methods. The values obtained, 41 ± 3% and 34 ± 2%, respectively, although smaller than the values already reported for downshifting multishell Nd^{3+}-based nanostructures are higher than those of semiconductor and metallic nanoparticles. The value recorded by the thermal relaxation method is slightly higher because the method neglects the light reflection and scattering from the sample and the cuvette in which the sample is contained. The thermal resistance of powder $KLu_{0.94}Ho_{0.01}Tm_{0.05}(WO_4)_2$ nanoparticles in contact with air, $(9.50 \pm 0.17) \times 10^7$ K W^{-1}, is of the same order of magnitude of that expected for interfacial thermal resistance Si nanorods and Si-based heterostructured nanowires. As the nanoparticles are in contact with each other, we can anticipate that the thermal resistance is dominated by the contact resistance at the interface between them. To study this effect, future work will be focused on the measurement of the dependence on the external pressure of the thermal resistance. Moreover, the role played by the medium in the thermal resistance can also be addressed by performing similar measurements in colloidal suspensions of the nanoparticles. In summary, all these new tools enlarge the application of luminescence thermometry paving the road to exploit the heat transfer processes occurring at the micro and nanoscale.

Conflicts of interest

There are no conflicts to declare.

Acknowledgements

This work has been supported by the Ministerio de Economía, Industria y Competitividad, the Agencia Estatal de Investigación (AEI) and the European Regional Development Fund (ERDF) under Projects No. TEC2014-55948-R and MAT2016-75716-C2-1-R (AEI/FEDER, UE), Secretaria d'Universitats i Recerca del Departament d'Economia i Coneixement de la Generalitat de Catalunya, the European Union (EU) and the European Social Fund (ESF) under Project No. 2017SGR755, and CMST COST Action CM1403, and partially developed in the scope of the project CICECO – Aveiro Institute of Materials (Ref. FCT UID/CTM/50011/2013), financed by Portuguese funds through the Fundação para a Ciência e a Tecnologia/Ministério da Educação e Ciência (FCT/MEC) and when applicable co-financed by FEDER under the PT2020 Partnership Agreement. Financial support of FCT (PTDC/CTM-NAN/4647/2014 and POCI-01-0145-FEDER-016687) is also acknowledged. OAS was supported by the Catalan Government through the fellowship 2015FI_B 00136, CDSB thanks the individual grant financed by the SusPhotoSolutions project CENTRO-01-0145-FEDER-000005, and FD acknowledges additional support through the ICREA Academia awards 2010ICREA-02 for excellence in research.

Notes and references

1 L. D. Carlos and F. Palacio, *Thermometry at the Nanoscale: Techniques and Selected Applications*, Royal Society of Chemistry, Oxfordshire, 2016.
2 K. Okabe, N. Inada, C. Gota, Y. Harada, T. Funatsu and S. Uchiyama, *Nat. Commun.*, 2012, **3**, 705.

3 J. S. Donner, S. A. Thompson, M. P. Kreuzer, G. Baffou and R. Quidant, *Nano Lett.*, 2012, **12**, 2107–2111.
4 G. Yang, X. Liu, J. Feng, S. Li and Y. Li, in *Thermometry at the nanoscale: techniques and selected applications*, ed. L. D. Carlos and F. Palacio, The Royal Society of Chemistry, 2016, vol. 38, ch. 6, pp. 167–189.
5 S. Kalytchuk, O. Zhovtiuk, S. V. Kershaw, R. Zboril and A. L. Rogach, *Small*, 2016, **12**, 466–476.
6 M. Back, E. Trave, J. Ueda and S. Tanabe, *Chem. Mater.*, 2016, **28**, 8347–8356.
7 C. D. S. Brites, P. P. Lima, N. J. O. Silva, A. Millán, V. S. Amaral, F. Palacio and L. D. Carlos, *Nanoscale*, 2013, **5**, 7572–7580.
8 G. Jalani, R. Naccache, D. H. Rosenzweig, L. Haglund, F. Vetrone and M. Cerruti, *J. Am. Chem. Soc.*, 2016, **138**, 1078–1083.
9 M. L. Debasu, C. D. S. Brites, S. Balabhadra, H. Oliveira, J. Rocha and L. D. Carlos, *ChemNanoMat*, 2016, **2**, 520–527.
10 X. Zhu, W. Feng, J. Chang, Y.-W. Tan, J. Li, M. Chen, Y. Sun and F. Li, *Nat. Commun.*, 2016, **7**, 10437.
11 O. A. Savchuk, P. Haro-González, J. J. Carvajal, D. Jaque, J. Massons, M. Aguiló and F. Diaz, *Nanoscale*, 2014, **6**, 9727–9733.
12 M. Bettinelli, L. D. Carlos and X. Liu, *Phys. Today*, 2015, **68**, 38–44.
13 V. Lojpur, M. G. Nikolić and M. D. Dramićanin, *J. Appl. Phys.*, 2014, **115**, 203106.
14 T. V. Gavrilović, D. J. Jovanović, V. Lojpur and M. D. Dramićanin, *Sci. Rep.*, 2014, **4**, 4209.
15 S. Balabhadra, M. L. Debasu, C. D. Brites, L. A. Nunes, O. L. Malta, J. Rocha, M. Bettinelli and L. D. Carlos, *Nanoscale*, 2015, **7**, 17261–17267.
16 Ł. Marciniak, A. Bednarkiewicz, M. Stefanski, R. Tomala, D. Hreniak and W. Strek, *Phys. Chem. Chem. Phys.*, 2015, **17**, 24315.
17 D. Jaque and F. Vetrone, *Nanoscale*, 2012, **4**, 4301–4326.
18 C. D. S. Brites, P. P. Lima, N. J. O. Silva, A. Millán, V. S. Amaral, F. Palacio and L. D. Carlos, *Nanoscale*, 2012, **4**, 4799–4829.
19 X. D. Wang, O. S. Wolfbeis and R. J. Meier, *Chem. Soc. Rev.*, 2013, **42**, 7834–7869.
20 C. D. S. Brites, A. Millán and L. D. Carlos, in *Handbook on the Physics and Chemistry of Rare Earths*, ed. J.-C. G. Bünzli and V. K. Pecharsky, Elsevier Science, B. V., Amsterdam, 2016, vol. 49, ch. 281, pp. 339–427.
21 M. Quintanilla, A. Benayas, R. Naccache and F. Vetrone, in *Thermometry at the nanoscale: techniques and selected applications*, ed. L. D. Carlos and F. Palacio, The Royal Society of Chemistry, Oxfordshire, 2016, vol. 38, ch. 5, pp. 124–166.
22 M. D. Dramićanin, *Methods Appl. Fluoresc.*, 2016, **4**, 042001.
23 E. Hemmer, P. Acosta-Mora, J. Mendez-Ramos and S. Fischer, *J. Mater. Chem. B*, 2017, **5**, 4365–4392.
24 B. Liu, C. X. Li, P. P. Yang, Z. Y. Hou and J. Lin, *Adv. Mater.*, 2017, **29**, 1605434.
25 T. Miyagawa, T. Fujie, Ferdinandus, T. T. V. Doan, H. Sato and S. Takeoka, *ACS Appl. Mater. Interfaces*, 2016, **8**, 33377–33385.
26 Ferdinandus, S. Arai, S. Takeoka, S. Ishiwata, M. Suzuki and H. Sato, *ACS Sens.*, 2016, **1**, 1222–1227.
27 E. C. Ximendes, U. Rocha, T. O. Sales, N. Fernández, F. Sanz-Rodríguez, I. R. Martín, C. Jacinto and D. Jaque, *Adv. Funct. Mater.*, 2017, 1702249.
28 E. C. Ximendes, U. Rocha, B. del Rosal, A. Vaquero, F. Sanz-Rodríguez, L. Monge, F. Ren, F. Vetrone, D. Ma and J. García-Solé, *Adv. Healthcare Mater.*, 2017, **6**, 1601195.
29 R. Piñol, C. D. S. Brites, R. Bustamante, A. Martínez, N. J. O. Silva, J. L. Murillo, R. Cases, J. Carrey, C. Estepa, C. Sosa, F. Palacio, L. D. Carlos and A. Millán, *ACS Nano*, 2015, **9**, 3134–3142.
30 E. C. Ximendes, W. Q. Santos, U. Rocha, U. K. Kagola, F. Sanz-Rodriguez, N. Fernandez, A. D. Gouveia-Neto, D. Bravo, A. M. Domingo, B. del Rosal, C. D. S. Brites, L. D. Carlos, D. Jaque and C. Jacinto, *Nano Lett.*, 2016, **16**, 1695–1703.
31 C. D. Brites, X. Xie, M. L. Debasu, X. Qin, R. Chen, W. Huang, J. Rocha, X. Liu and L. D. Carlos, *Nat. Nanotechnol.*, 2016, **11**, 851–856.
32 C. D. S. Brites, M. C. Fuertes, P. C. Angelomé, E. D. Martínez, P. P. Lima, G. J. A. A. Soler-Illia and L. D. Carlos, *Nano Lett.*, 2017, **17**, 4746–4752.
33 J. Verma, S. Lal and C. J. F. Van Noorden, *Int. J. Nanomed.*, 2014, **9**, 2863–2877.
34 D. de Melo-Diogo, C. Pais-Silva, D. R. Dias, A. F. Moreira and I. J. Correia, *Adv. Healthcare Mater.*, 2017, **6**, 1700073.
35 U. Rocha, K. U. Kumar, C. Jacinto, J. Ramiro, A. J. Caamano, J. G. Solé and D. Jaque, *Appl. Phys. Lett.*, 2014, **104**, 053703.
36 D. Jaque, L. M. Maestro, B. Del Rosal, P. Haro-Gonzalez, A. Benayas, J. Plaza, E. M. Rodríguez and J. G. Solé, *Nanoscale*, 2014, **6**, 9494–9530.
37 A. K. Silva, A. Nicolas-Boluda, L. Fouassier and F. Gazeau, *Nanomedicine*, 2017, **12**, 1213–1215.
38 N. Lee, D. Yoo, D. Ling, M. H. Cho, T. Hyeon and J. Cheon, *Chem. Rev.*, 2015, **115**, 10637–10689.
39 D. Wawrzynczyk, A. Bednarkiewicz, M. Nyk, W. Strek and M. Samoc, *Nanoscale*, 2012, **4**, 6959–6961.
40 M. L. Debasu, D. Ananias, I. Pastoriza-Santos, L. M. Liz-Marzán, J. Rocha and L. D. Carlos, *Adv. Mater.*, 2013, **25**, 4868–4874.
41 U. Rocha, C. Jacinto da Silva, W. Ferreira Silva, I. Guedes, A. Benayas, L. Martínez Maestro, M. Acosta Elias, E. Bovero, F. C. J. M. van Veggel, J. G. Solé and D. Jaque, *ACS Nano*, 2013, **7**, 1188–1199.
42 E. Carrasco, B. del Rosal, F. Sanz-Rodríguez, Á. J. de la Fuente, P. H. Gonzalez, U. Rocha, K. U. Kumar, C. Jacinto, J. G. Solé and D. Jaque, *Adv. Funct. Mater.*, 2015, **25**, 615–626.
43 O. A. Savchuk, J. J. Carvajal, C. Cascales, M. Aguiló and F. Diaz, *ACS Appl. Mater. Interfaces*, 2016, **8**, 7266–7273.

44 L. L. Xing, Y. L. Xu, R. Wang, W. Xu and Z. G. Zhang, *Opt. Lett.*, 2014, **39**, 454–457.
45 L. Marciniak, A. Bednarkiewicz, D. Kowalska and W. Strek, *J. Mater. Chem. C*, 2016, **4**, 5559–5563.
46 L. Marciniak, K. Prorok, A. Bednarkiewicz, A. Kowalczyk, D. Hreniak and W. Strek, *J. Lumin.*, 2016, **176**, 144–148.
47 A. Benayas, B. del Rosal, A. Perez-Delgado, K. Santacruz-Gomez, D. Jaque, G. A. Hirata and F. Vetrone, *Adv. Opt. Mater.*, 2015, **3**, 687–694.
48 M. Pedroni, P. Cortelletti, I. X. Cantarelli, N. Pinna, P. Canton, M. Quintanilla, F. Vetrone and A. Speghini, *Sens. Actuators, B*, 2017, **250**, 147–155.
49 P. Cortelletti, C. Facciotti, I. X. Cantarelli, P. Canton, M. Quintanilla, F. Vetrone, A. Speghini and M. Pedroni, *Opt. Mater.*, 2017, **68**, 29–34.
50 L. Marciniak, A. Pilch, S. Arabasz, D. Jin and A. Bednarkiewicz, *Nanoscale*, 2017, **9**, 8288–8297.
51 B. del Rosal, U. Rocha, E. C. Ximendes, E. M. Rodriguez, D. Jaque and J. G. Sole, *Opt. Mater.*, 2017, **63**, 185–196.
52 B. del Rosal, A. Perez-Delgado, E. Carrasco, D. J. Jovanovic, M. D. Dramicanin, G. Drazic, A. J. de la Fuente, F. Sanz-Rodriguez and D. Jaque, *Adv. Opt. Mater.*, 2016, **4**, 782–789.
53 O. A. Savchuk, J. Carvajal, J. Massons, M. Aguiló and F. Díaz, *Carbon*, 2016, **103**, 134–141.
54 D. K. Roper, W. Ahn and M. Hoepfner, *J. Phys. Chem. C*, 2007, **111**, 3636–3641.
55 R. Prasher, *Nano Lett.*, 2005, **5**, 2155–2159.
56 M. Galceran, M. Pujol, M. Aguiló and F. Díaz, *J. Sol-Gel Sci. Technol.*, 2007, **42**, 79–88.
57 O. A. Savchuk, J. J. Carvajal, M. C. Pujol, E. W. Barrera, J. Massons, M. Aguilo and F. Diaz, *J. Phys. Chem. C*, 2015, **119**, 18546–18558.
58 S. A. Payne, L. K. Smith, W. L. Kway, J. B. Tassano and W. F. Krupke, *J. Phys.: Condens. Matter*, 1992, **4**, 8525.
59 M. Guan, H. Zheng, L. Mei, Z. Huang, T. Yang, M. Fang and Y. Liu, *Infrared Phys. Technol.*, 2014, **67**, 107–110.
60 Y. Li, Y. Wang, B. Yao and Y. Liu, *Laser Phys. Lett.*, 2008, **5**, 597.
61 A. C. Brandão-Silva, M. A. Gomes, S. M. V. Novais, Z. S. Macedo, J. F. M. Avila, J. J. Rodrigues and M. A. R. C. Alencar, *J. Alloys Compd.*, 2018, **731**, 478–488.
62 Z. Wang, R. Xie, C. T. Bui, D. Liu, X. Ni, B. Li and J. T. Thong, *Nano Lett.*, 2010, **11**, 113–118.
63 Z. An, M. Toda and T. Ono, *Carbon*, 2014, **75**, 281–288.
64 G. Hwang and O. Kwon, *Nanoscale*, 2016, **8**, 5280–5290.
65 Y. K. Koh and D. G. Cahill, *Phys. Rev. B: Condens. Matter Mater. Phys.*, 2007, **76**, 075207.
66 F. P. Incropera, D. P. DeWitt, T. L. Bergman and A. S. Lavine, *Introduction to Heat Transfer*, Wiley, New York, 5 edn, 2006.
67 J. H. Lienhard, *A heat transfer textbook*, Courier Corporation, 2013.
68 M. Pujol, X. Mateos, A. Aznar, X. Solans, S. Surinach, J. Massons, F. Díaz and M. Aguiló, *J. Appl. Crystallogr.*, 2006, **39**, 230–236.
69 Ò. Silvestre, J. Grau, M. C. Pujol, J. Massons, M. Aguiló, F. Díaz, M. T. Borowiec, A. Szewczyk, M. U. Gutowska and M. Massot, *Opt. Express*, 2008, **16**, 5022–5034.
70 D. Liu, R. G. Xie, N. Yang, B. W. Li and J. T. L. Thong, *Nano Lett.*, 2014, **14**, 806–812.
71 E. Saïdi, N. Babinet, L. Lalouat, J. Lesueur, L. Aigouy, S. Volz, J. Labeguerie-Egea and M. Mortier, *Small*, 2011, **7**, 259–264.
72 J.-P. Tetienne, A. Lombard, D. A. Simpson, C. Ritchie, J. Lu, P. Mulvaney and L. C. Hollenberg, *Nano Lett.*, 2016, **16**, 326–333.
73 I. Sedmak, I. Urbancic, J. Strancar, M. Mortier and I. Golobic, *Sens. Actuators, A*, 2015, **230**, 102–110.
74 V. V. Deshpande, S. Hsieh, A. W. Bushmaker, M. Bockrath and S. B. Cronin, *Phys. Rev. Lett.*, 2009, **102**, 105501.
75 C. D. S. Brites, P. P. Lima, N. J. O. Silva, A. Millán, V. S. Amaral, F. Palacio and L. D. Carlos, *Front. Chem.*, 2013, **1**, 9.
76 R. A. S. Ferreira, C. D. S. Brites, C. M. S. Vicente, P. P. Lima, A. R. N. Bastos, P. G. Marques, M. Hiltunen, L. D. Carlos and P. S. André, *Laser Photonics Rev.*, 2013, **7**, 1027–1035.